

Effect of surface alignment on channel connectivity of phosphonium-containing diblock copolymer anion exchange membranes

Austin M. Barnes,^{†+} Yifeng Du,^{‡+} Brendan Liu,[†] Wenxu Zhang,[‡] Soenke Seifert,¹ E. Bryan

Coughlin,[‡] Steven K. Buratto^{†*}

[†]Department of Chemistry and Biochemistry, University of California, Santa Barbara, California 93106-9510, United States

[‡]Department of Polymer Science and Engineering, University of Massachusetts Amherst, 120 Governors Drive, Amherst, Massachusetts 01003, United States

¹X-Ray Science Division, Argonne National Laboratory, Argonne, Illinois 60439, United States

⁺Authors contributed equally

ABSTRACT

The performance of ion exchange membranes in fuel cells is critically linked to its ion-conducting channel morphology. In this report, we analyzed the channel connectivity of anion exchange membranes (AEMs) by electrostatic force microscopy (EFM). As a tapping-mode AFM based technique, EFM probes height, phase, and electrostatic force gradient images through two-pass interleave scans, which reveals the direct relationship between membrane surface morphology and channel connectivity. The AEMs are diblock copolymers of a polyisoprene (PIp) block and a polystyrenic block containing phosphonium ion ($P(R_3P^+)MS$). Different alignments of cylinders were observed in bulk and on surface for AEMs with different ion exchange capacity (IEC) and preparation methods. The impacts of the cylinder alignment on the channel connectivity were then investigated by EFM. For AEM 13 with parallel aligned cylinders on the surface, many disconnected channels were observed throughout the membrane. In contrast, the perpendicularly aligned channels of AEM 16 consisted only of connected channels.

INTRODUCTION

Anion exchange membrane (AEM) fuel cells have garnered significant research interest in the past decades due to the improved cathode reaction kinetics under an alkaline environment.¹⁻³ Compared to the acidic environment of proton exchange membrane (PEM) fuel cells, AEM allows for reduced loading of expensive platinum catalyst or replacement by silver or gold.⁴ Despite of the similar transport mechanisms in both AEMs and PEMs,⁵ including Grotthuss mechanism,^{6,7} surface-site hopping,^{7,8} and diffusion,⁹ AEMs exhibit lower conductivity at current stage of

development. In pursuit of higher conductivity, a fundamental study on membrane structure-property relationship is in need. Nafion is the current state-of-the-art PEM and a benchmark for future membrane development, however, its random sulfonated backbone structure makes interpretation of scattering data difficult. Although several models have accurately described the scattering characteristics, they are still under debate.¹⁰⁻¹² On the contrary, ion-containing block copolymers provide tunable ordered morphologies, thus, can serve as a model system for the morphology-channel connectivity study, which leads to the ultimate goal of achieving a favorable ion transport environment and improving conductivity.

In this study, quaternary phosphonium (QP) containing diblock copolymers were synthesized. Polyisoprene (PIp) was chosen as the hydrophobic block because of the low glass-transition temperature (T_g), therefore, PIp provides the membrane attendant flexibility. The bulky phosphonium pedant group was chosen to implement on the ionic block, because the bulky cation can effectively hinder the hydroxyl attack, thus, greatly improve the chemical stability of AEMs in alkaline conditions.^{13,14} By modulating molecular weights of two blocks, a range of IEC (0.40-0.92 mmol/g) were achieved. Due to the Coulombic interactions from the charged block copolymer, inverse hexagonal morphology was observed for all AEMs, where the ionic block formed the continuous phase.¹⁵ However, parallel-aligned cylinders were observed on surface at AEM 13 with a moderate IEC (~0.44 mmol/g), while as for AEM 16 with a high IEC (~0.87 mmol/g), hexagonal morphologies showed perpendicular alignment, according to atomic force microscopy (AFM). What remains to be seen is how the alignment of surface domains influences channel connectivity. Although it has been hypothesized that parallel alignment can impede charge transport at the membrane-electrode interface,¹⁶ there has so far been no direct supporting evidence.

The channel structures and connectivity of AEM 13 and 16, with different surface morphologies, were investigated by electrostatic force microscopy (EFM). As a tapping-mode AFM based technique, EFM probes the electrostatic force gradient based on two-pass interleave scan. In the 1st pass, phase deviations depend on whether the tip-sample interactions are attractive ($>90^\circ$) or repulsive ($<90^\circ$).¹⁷ Tip-sample power dissipation is related to the sine of the phase angle, hence phase deviations toward 90° in both attractive and repulsive-mode imply maximum power dissipation.¹⁸ All of our phase images were gathered in repulsive mode. In the 2nd pass, phase deviations are influenced by the electrostatic force gradient, which is attributed to surface charge, dielectric permittivity, and film capacitance. EFM has been used to investigate the surface charge characteristics of isolated nanostructures¹⁹⁻²² and structures imbedded in thin films.^{23,24} Previously, EFM has been demonstrated to be a useful tool to study the disconnected dead-end channels in Nafion.²⁵ In this work, we compared the EFM vs. voltage bias response between parallel-aligned cylindrical channels and perpendicularly-aligned ones. Supported by previously established models of isolated structures,²⁶ variation in EFM phase with respect to change in bias voltage is indicative of regions where charge is trapped due to the disconnection in channels. Thus, from different EFM responses as a function of bias voltage, the channel structures and connectivity can be evaluated. These findings provide direct evidence of the relationship between membrane preparation methods, morphology and channel connectivity, which in turn helps direct the synthesis and processing methods of these promising AEM materials.

METHODS AND MATERIALS

Membrane Casting. For drop-casted membranes, the solution of quaternized diblock copolymer, PIp- $P(R_3P^+)MS$, in chloroform (~50 mg/ml, 1ml) was drop-cast onto a clean

polytetrafluorethylene sheet and dried slowly overnight. The membranes were then solvent-annealed by THF vapor for 24 h before peeling off the substrate and stored in a vial prior to bulk and surface characterization. The thicknesses of the membranes, measured by AFM, were $\sim 6 \mu\text{m}$. For spun-cast membranes, the membranes were spun-cast on a conductive fluorine-doped tin oxide (FTO) substrate. Only AEM 16 was spun-cast, which is denoted by AEM 16-SC. It is important to note that attempts were made to spin-cast AEM 13 for comparison. However, the low availability of this membrane from prior synthesis led to non-uniform film thicknesses and a disappearance of the parallel cylinder structure. FTO was cut into 2x2 cm squares. The substrates were cleaned by sonicating in a 1:1 EtOH/DI bath for 15 minutes followed by a DI bath for 15 minutes. FTO was then air-dried in petri-dish. As-received membranes were re-cast by tetrahydrofuran (THF). A 5% wt. solution was sonicated for 5 minutes and spun-cast on clean FTO at 3000 rpm. The thicknesses of the membranes were measured by AFM to be $\sim 40 \text{ nm}$.

Small Angle X-Ray Scattering (SAXS). SAXS measurements were performed using a GANESHA 300 XL SAXS. Humidity-dependent SAXS measurements were performed at The Basic Energy Sciences Synchrotron Radiation Center (BESSRC) at the Advanced Photon Source at Argonne National Lab on beamline 12 ID-B. A Pliatus 2M SAXS detector was used to collect scattering data with an exposure time of 1 s. The X-ray beam had a wavelength of 1 \AA and power of 12 keV. The intensity (I) is a radial integration of the 2D scattering pattern with respect to the scattering vector (q).

Transmission Electron Microscopy (TEM). The TEM specimens were prepared by Leica CryoUltramicrotome. The microtome chamber was cooled down to $-100 \text{ }^\circ\text{C}$ by liquid nitrogen, where the bulk sample was microtomed by diamond knife with the thickness around 40 nm. The cutting sections were then collected by 400 mesh copper support grids and stained by OsO_4 vapor for 20 min under room temperature. TEM characterization was performed on a JEOL 2000FX TEM operated at an accelerating voltage of 200 kV.

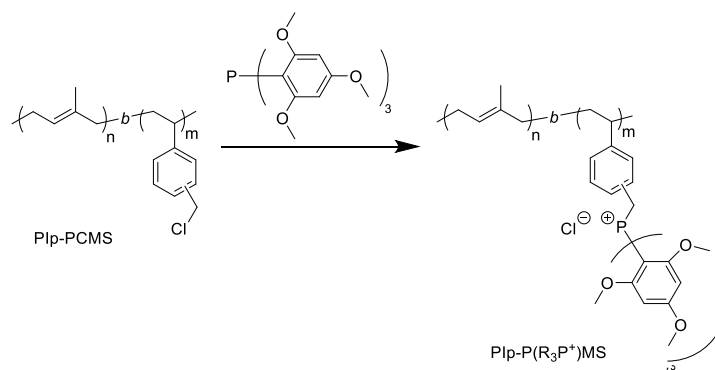
Atomic Force Microscopy (AFM). Height and phase images were acquired in tapping mode using an atomic force microscope (Asylum Research MFP3D). Standard silicon probes (XSC11, Mikromasch) with resonant frequency ($\sim 300 \text{ kHz}$) and spring constant (40 N/m) were used. The power spectral densities (PSDs) were computed in Gwyddion and plotted in Igor Pro. PSDs were collected over 5 different regions corresponding to a different image. The position of the peak indicates the maximum spatial frequency of the AFM phase images. We identify the 1st peak (q) in the PSD. The d-spacing is defined as $\frac{2\pi}{q}$.

Electrostatic Force Microscopy (EFM). EFM is an amplitude contrast tapping mode AFM technique based on two-pass interleave scan in which height and phase are measured in the 1st pass and a lift height of 20 nm is applied to the tip in the 2nd pass. A constant DC bias is applied to the electrode substrate while the tip is held at ground. A Pt-coated tip provided by Mikromasch (model HQ:XSC11/Pt) with a resonant frequency of $\sim 325 \text{ kHz}$, and tip radius of curvature $< 27 \text{ nm}$ was used. We scanned the same region for different voltage biases applied to the substrate from the microscope controller. We applied 0V, +/-1V, +/-3V, and +/- 5V. The measurements were done under ambient conditions (30-50% RH) and at room temperature. All the images were acquired using the retrace image. The (x,y) position of the domains in the phase image were marked by a cursor which highlights the (x,y) position in the EFM images. Domains that appeared to be

influenced by roughness in the height image were neglected. A more detailed description of how height-artifacts are neglected are described in the supporting information. The EFM phase as a function of V_{EFM} ($V_{\text{EFM}} = V_{\text{tip}} - V_{\text{substrate}}$) was plotted for each domain and was fit to a 3rd order polynomial.

RESULTS AND DISCUSSION

Scheme 1: Synthesis of Phosphonium-containing Diblock Copolymer



Zhang *et al.* synthesized quaternary phosphonium (QP) contained diblock copolymers by reversible addition – fragmentation chain-transfer (RAFT).¹⁴ The parental neutral block polymer consists of polyisoprene (PIp) block and polychloromethylstyrene (PCMS) block, whose benzylic positions provide quaternizable sites. As shown in Scheme 1, excess quaternization agents, tris(2,4,6-trimethoxyphenyl) phosphine ($\text{P}(\text{Ph}(\text{OMe})_3)_3$) was added to react with PCMS. After quaternization, the neutral-charged block copolymer, polyisoprene-poly(trimethoxyphenylphosphinemethylstyrene) (PIp-P(R_3P^+)MS), where $\text{R} = \text{P}(\text{Ph}(\text{OMe})_3)_3$, was obtained. The theoretical ion exchange capacities (IEC) was determined based on the volume fraction of PCMS block and the quaternization efficiency. PIp-P(R_3P^+)MS with IEC ranging from 0.3 to 0.6 mmol/g were synthesized.¹⁴ We have also recently synthesized PIp-P(R_3P^+)MS diblock copolymer membranes by nitroxide mediated polymerization (NMP), which provided faster polymerization dynamic and larger degree of polymerization of PCMS block. After quaternization, higher IECs of 0.87-0.92 mmol/g was achieved.

The following investigation involves specifically with AEM 13 (IEC = 0.44 mmol/g) and AEM 16 (IEC = 0.87 mmol/g). Bulk morphologies were investigated by SAXS and TEM, as shown in [Fig-Figure 1](#). SAXS profiles of the AEM 13 and 16 are shown in [Fig-Figure 1A](#) and [1E](#), respectively. [Figure 1A](#) (AEM 13) shows scattering peak positions at q , $\sqrt{3}q$, and $\sqrt{7}q$, while [Figure 1E](#) (AEM 16) shows peak positions at q and $\sqrt{3}q$. Both peak positions are indicative of hexagonal cylinder morphology. The orientation of the cylindrical domains was assessed by cross-sectional TEM. Figure [1B](#) and [1F](#) show cross-sectional TEM of the bulk structure of AEM 13 and AEM 16, respectively. Prior to TEM, the membranes were microtomed by ~ 40 nm thick and stained by OsO_4 , which selectively stains [the \$\alpha\$ -PIp block](#). Therefore, the dark contrast indicates the hydrophobic PIp domains. In [Figure 1B](#), a mixture of perpendicular and parallel

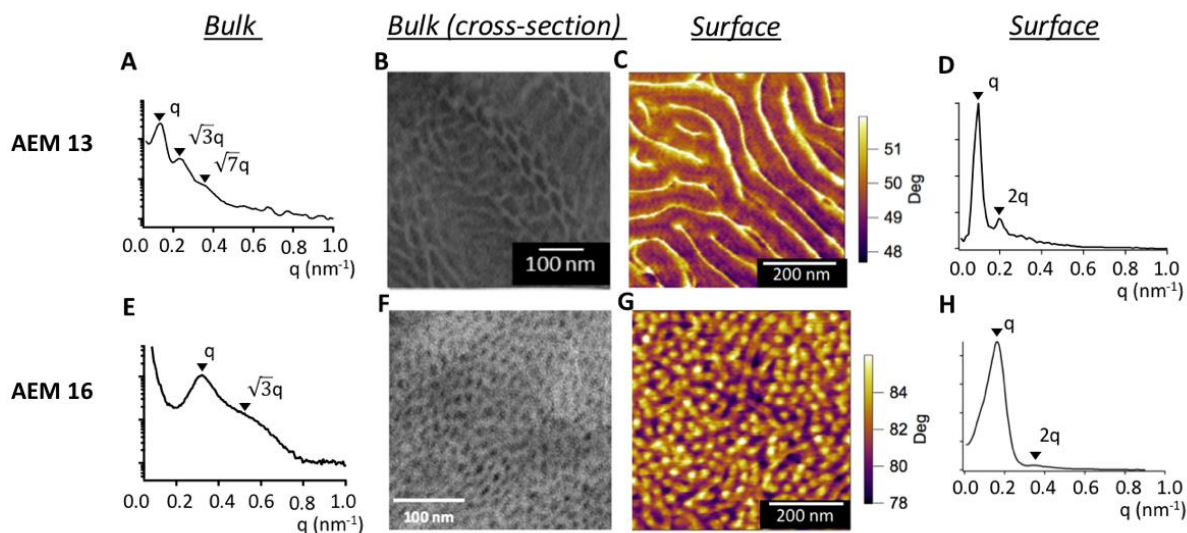


Figure 1: Comparison of the bulk (internal) structure and surface structure of AEM 13 and AEM 16. SAXS of (A) AEM 13 and (E) AEM 16, with peak labeled, both indicating hexagonal morphology. Cross-sectional TEM of (B) AEM 13 and (F) AEM 16, where dark contrast corresponds to PIp domains. Repulsive mode phase images of (C) AEM 13 and (G) C, where dark contrast corresponds to PIp domains. Radially-averaged power spectral density (PSD) of phase images of (D) AEM 13 and (H) AEM 16, with higher order peak at $2q$ labelled.

aligned cylinders were observed. The surface morphology was revealed by AFM. The phase images were collected in repulsive mode. We have interpreted the bright contrast as the ionic $\text{P}(\text{R}_3\text{P}^+)\text{MS}$ domains and the dark contrast as the hydrophobic PIp domains. By imaging partially quaternized membranes, we have indicated that the bright regions are associated with the ionic domains, as shown in the Supporting Information. Figure [1C](#) and [1G](#) are phase images of AEM 13 and spun-cast AEM 16 (AEM16-SC), respectively. The images show stark differences between the surface alignment. [Figure 1C](#) shows cylinders forming parallel to the surface, while [Figure 1G](#) indicates perpendicularly aligned cylinders. This implies that in AEM 13, perpendicular channels convert to parallel channels at the surface as the film dries. In AEM 16, on the other hand, shows perpendicular alignment of the channels. By spin-casting AEM 16, we are able to freeze the bulk morphology at the surface. This gives us a means of comparing the conductive properties of two different surface morphologies for AEMs with similar bulk morphologies. Surface alignment was further confirmed by PSD analysis for both AFM phase images, as shown in [Figure 1D](#) and [1H](#),

respectively. The PSD is useful in analyzing spatial frequencies of AFM images. Surface ordering information of block copolymer membrane films through analysis of peak positions of higher order peaks relative to the primary peak.^{27,28} In [Figure 1C](#), the peaks are positioned at q and $2q$, which signifies regular periodic order typically observed in lamellar phases. In [Figure 1H](#), the peak positions for AEM 16 are also q and $2q$ with the higher order peak is much less intense, signifying short-range order.

Domain sizes and spacing can be measured from the bulk and surface, respectively. For AEM 13, the average diameter of the PIP domains within the bulk was measured by TEM to be 40 nm, in agreement with the d -spacing ~ 42 nm calculated from SAXS. On the surface, the cylinders were 60 nm in width by measuring several line profiles from AFM. The surface d -spacing can also be calculated from the PSD of the phase images, defined as $d = \frac{2\pi}{q}$, where q is the primary peak. From 1D, the d -spacing was 61 nm, corresponding approximately to the widths of the cylinders measured by line profiles. In AEM 16, however, similar domain sizes were observed from both the bulk and the surface. From the TEM image in [1F](#), the average diameter was 20 nm. This is comparable with the d -spacing from SAXS shown in [Figure 1E](#), which was 23 nm. On the surface, the average diameter of the bright and dark domains in [Figure image-1G](#) was 17 nm and 19.8 nm, respectively. The d -spacing from the PSD shown in [1H](#) is 36.7 nm, which indicates close agreement of surface d -spacing with that in bulk.

The surface free energy difference between two blocks in block copolymers influences the alignment of domains at the air-membrane interface.²⁹⁻³¹ A cartoon illustration of the proposed channel structures due to alignment difference is shown in [Figure 2](#). Mixed alignment of PIP cylinders in the bulk with parallel alignment on surface for AEM 13, shown in [2A](#). The left side of the cartoon of [2A](#) shows a misaligned surface domain with respect to the bulk domain. It is possible that this misalignment can result in a dead-end channel, i.e. one that blocks charge from reaching the air-membrane interface. The right side of the cartoon of [2A](#) shows a properly aligned surface channel with that of the bulk. This case results in connected channels that allow charge to migrate contiguously throughout the entire membrane. Thus, the conductivity of block copolymer AEMs is dependent on channel alignment at the surface.¹⁶ [Figure 2B](#) illustrates that at high volume fraction of the $P(R_3P^+)MS$ block, the cylinders only align perpendicular to the air-membrane interface throughout the membrane, leading solely connected channels.

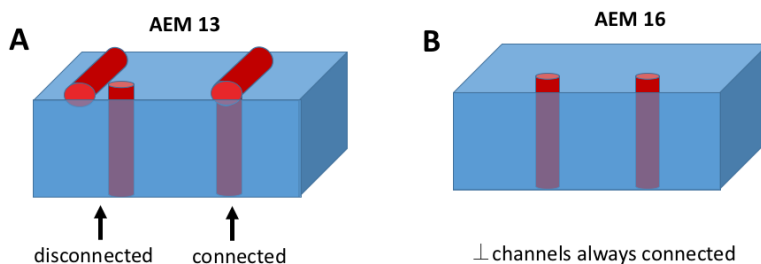


Figure 2: Cartoons illustrating the proposed structure leading to variation in channel connectivity. The red cylinders represent the PIp phase while blue represents the continuous ionic phase. (A) Low volume fraction of the ionic block gives rise to parallel aligned cylinders. This orientation can either block surface charge migration, or provide a connected path. (B) At high volume fraction, cylinders are aligned perpendicularly, which gives rise to only connected paths.

solvent vapor annealing can trap the block copolymer in a non-equilibrium morphology.³² In drop-cast films, the solvent evaporates slowly (over 6 h) under ambient RH, which favors the formation of larger ionic domains on the surface than bulk. In spun-cast films, the bulk structure is trapped at the surface because the film is not given enough time to reach equilibrium at ambient RH, thus giving rise to smaller ionic domains distributed on surface. Since the alignment, ordering, and size of domains at the surface of spun-cast AEM 16 are commensurate with bulk measurements of drop-cast AEM 16, we use AEM 16 as a benchmark hexagonal membrane with well-connected channels to compare with AEM 13. Furthermore, the similarities in bulk morphologies of AEM 13 and AEM 16 make them good candidates for comparing the influence of different surface alignments on charge migration and channel connectivity.

EFM is a tapping-mode AFM based technique that probes the electrostatic force gradient. EFM is based on two-pass interleave scan. In the 1st pass, the height and phase are gathered. In the 2nd pass, phase deviations are influenced by the electrostatic force gradient, which is attributed to surface charge, dielectric permittivity, and film capacitance. The conductive tip is raised above the surface by 20 nm. A constant DC bias is applied to the electrode FTO sample substrate (V_{sample}) while the platinum-coated tip is held at ground ($V_{\text{tip}} = 0$). Conventionally, the bias voltage is defined as $V_{\text{EFM}} = V_{\text{tip}} - V_{\text{sample}}$. Hence, $V_{\text{EFM}} = -V_{\text{sample}}$. The ions migrate depending on the sign of the bias voltage, for example, a $V_{\text{EFM}} = +5\text{V}$ implies a negative sample voltage and would bias the ions toward the surface. Figure 3A and 3D shows 1st pass phase images of AEM 13 and AEM 16 showing the same morphologies from images shown in Figure 1. Figure 3B and 3C shows EFM images of AEM 13 at -5V and +5V FTO sample bias, respectively. Although the difference in thickness of the two membranes can affect capacitive interaction of the tip-sample system, we showed in the Supporting Information that this only leads to a small offset relative to the difference in IEC.

Different sample preparation methods play a significant role in affecting bulk and surface morphologies, via different film formation kinetics.^{32,33} AEM 13 was prepared by drop-casting from CHCl_3 solution onto a PTFE sheet. AEM 16 was spun-cast from THF solution onto a fluorine doped tin oxide (FTO) substrate. Drop-cast films were $\sim 6 \mu\text{m}$ thick while spun-cast films were $\sim 40 \text{ nm}$ thick. It has been demonstrated that film deposition by fast solvent extraction via spin-casting or

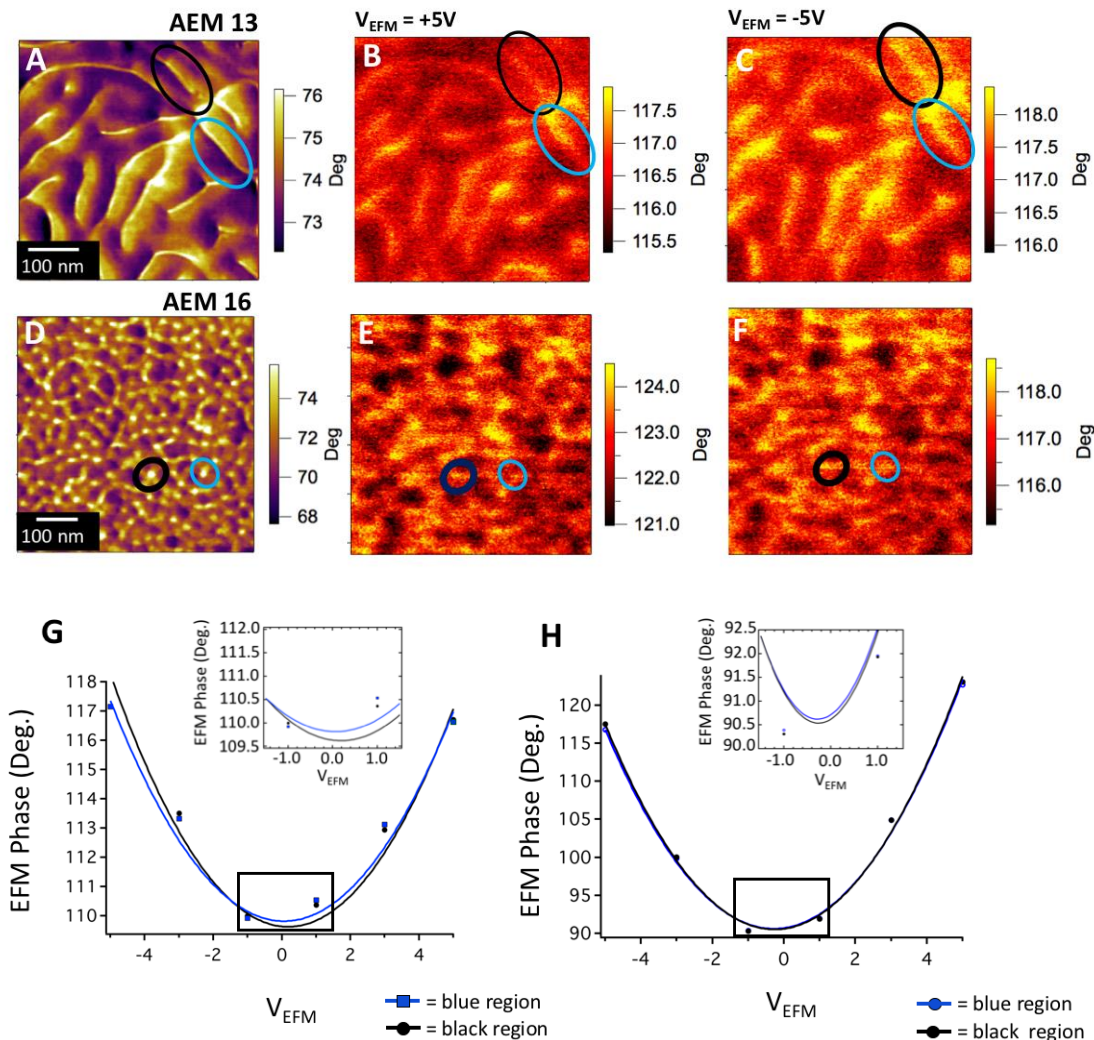


Figure 3: (A) 1st pass repulsive-mode phase image of as-received AEM 13. EFM images taken in the 2nd pass at (B) $V_{EFM} = +5V$ and (C) $V_{EFM} = -5V$ sample bias. (D) Repulsive-mode phase image of AEM 16-SC taken in the 1st pass. EFM images taken in the 2nd pass at (E) $-5V$ sample bias and (F) $+5V$ sample bias. Parabolic response of EFM phase as a function of V_{EFM} ($V_{EFM} = V_{tip} - V_{sample}$) for two regions highlighted (G) in images 3A-C of AEM 13 and (H) in 3D-F and AEM 16.

Two representative ionic regions of AEM 13 are highlighted in [Figure 3A-C](#). The EFM phase was determined by drawing a square box (20 nm x 20 nm) over the ionic region of interest in the 1st pass phase image in Igor Pro. The (X,Y) spatial coordinates in the 1st pass correspond to the same coordinates in the 2nd pass EFM phase image, and therefore the square box can be copied onto the 2nd pass EFM image. The statistical average was measured over ~100 pixels contained in the square box. This method was applied to the same ionic region of interest for each voltage bias.

For example, the blue highlighted region shows a small uniform shift (-0.5°) in EFM phase between the +5V and -5V image while the black region shows a larger and more negative shift (-1.5°) between the two images. A different EFM phase response as a function of voltage bias was observed for AEM 16. Figure 3D shows a repulsive mode phase image of AEM 16. Similar EFM phase contrast can be seen in blue and black highlighted regions at both voltage biases (Figure 3E and 3F), showing a uniform shift in the EFM phase ($+5.9^\circ$) with respect to voltage bias for both regions. Besides, a higher EFM phase shift was observed as expected, since AEM 16 has larger IEC, allowing larger population of charges to be biased towards the surface, which leads to a larger positive shift. Heterogeneity in the EFM phase of AEM 13 can be attributed to “dead-end” ionic channels due to the parallel hydrophobic cylinders that block the chloride from reaching the surface, while homogeneity for AEM 16 can be attributed to identical connected channel structures.

It is important to note that the sign of the shift does not provide adequate information on the channel structure, thus the parabolic EFM behavior of the channels must be analyzed. EFM phase shifts as a function of the bias voltage and can be described mathematically via Equation 1.³⁴

$$\Delta\Phi = -\frac{Q}{2k} \frac{d^2C}{dz^2} [(V_{EFM} - V_s)^2 - 2(V_{EFM} - V_s)V_q + V_q^2] \quad (1)$$

where Q is the quality factor of the cantilever, k is the spring constant of the cantilever, C is the capacitance of the tip-sample system, z is the height above the surface. V_{EFM} is the bias voltage ($V_{EFM} = V_{tip} - V_{sample}$). V_s is the surface potential, which is related to the work function difference between the tip and the sample and is independent of the lift height. We consider V_s to be a constant offset potential and is independent of V_{EFM} . V_q is the potential related to the charge enclosed and is dependent on the lift height. The first term in Eq. (1) is related to the tip-sample capacitance and induced polarization of the film, which is always an attractive force. The middle term in Eq. (1) is related to the interaction between the stored charge, q and the EFM tip apex. The third term is related to the image charge effects, since this is independent of V_{EFM} , we have ignored this interaction from analysis. We can simplify the expression for Eq. (1) into two terms: a charge force gradient ($\Delta\Phi_q$) that has a linear dependence on V_{EFM} and a capacitive force gradient ($\Delta\Phi_C$) that has a quadratic dependence with V_{EFM} .

$$\Delta\Phi = \Delta\Phi_q + \Delta\Phi_C = AV_{EFM} + BV_{EFM}^2 \quad (2)$$

A and B are fitting parameters to the linear and quadratic terms, respectively. For a charged dielectric film placed in a uniform electric field, the quadratic and linear terms are derived analytically in the Supporting Information.

$$B = \frac{Q}{2k} \left(\frac{3\alpha}{(z+d)^4} \right) \quad (3)$$

$$A = \frac{-Qq}{2k(z+d)^3} \quad (4)$$

Where α is the electric polarizability, d is the film thickness, and q is the stored charge.

For the blue region highlighted in AEM 13, the average EFM phase was measured for each voltage bias and plotted as blue squares shown in 3G. The method of measuring the EFM phase was the same method previously described.²⁵ The data was fit to a quadratic function and the fit curve is shown as the blue line. Similarly, the black region in AEM 13 was plotted as black circles and fit to a quadratic function shown as the black line. In 3G, there are noticeable differences between the blue and black fits. The insets show a close-up of the differences. Furthermore, the analytical expressions shown in Eq. (3) and (4) can be simplified by taking the ratio of A and B, which is dependent on stored charge (q), film thickness (d), and polarizability (α).

$$\frac{A}{B} = \frac{-q(z+d)}{3\alpha} \quad (5)$$

Note [Eq. \(5\)](#) is similar for the ratio expression derived for EFM studies of Nafion.²⁵ The EFM phase of Nafion was background subtracted and assumptions regarding the relative permittivity and the charge density of the ionic domains allowed for simplified expressions. Heterogeneity in the A and B fits were due to differences in channel length or geometry. In this investigation, we can draw similar conclusions, however, we are comparing two membranes of different charge density (IEC) and film thickness. Therefore, the EFM phase was not background subtracted and the film thickness (d) is included in the expression, which represents a pocket of charge or a connected channel plus the remaining thickness of the film. The relative permittivity of the ionic domains is also not known. Hence, B was expressed in terms of the polarizability of the film.

For the blue curve, the fitting parameters were $A = -0.036^\circ/V$ and $B = 0.294^\circ/V^2$. Thus, A/B is calculated to be -0.122 V. For the black curve in 3G, $A = -0.118^\circ/V$, $B = 0.321^\circ/V^2$, and $A/B = -0.368$ V. The differences in A/B between these two regions supports our qualitative depictions shown in 2C. The black region in AEM 13 shows a large negative A/B which signifies a “dead-end” channel, while the blue region shifts to less negative, signifying a connected channel. Both A/B values are negative, which could be due to a negative surface potential, V_s , the potential in the absence of stored charge shown in Eq. (1). The same analysis was performed on AEM 16. First, smaller deviation was observed in 3H between quadratic fits for blue and black regions highlighted in images 3D-F. For region 1, $A = 0.632^\circ/V$ and $B = 1.201^\circ/V^2$. For region 2, $A = 0.661^\circ/V$ and $B = 1.176^\circ/V^2$. A/B for these regions are 0.525 V and 0.562 V, respectively.

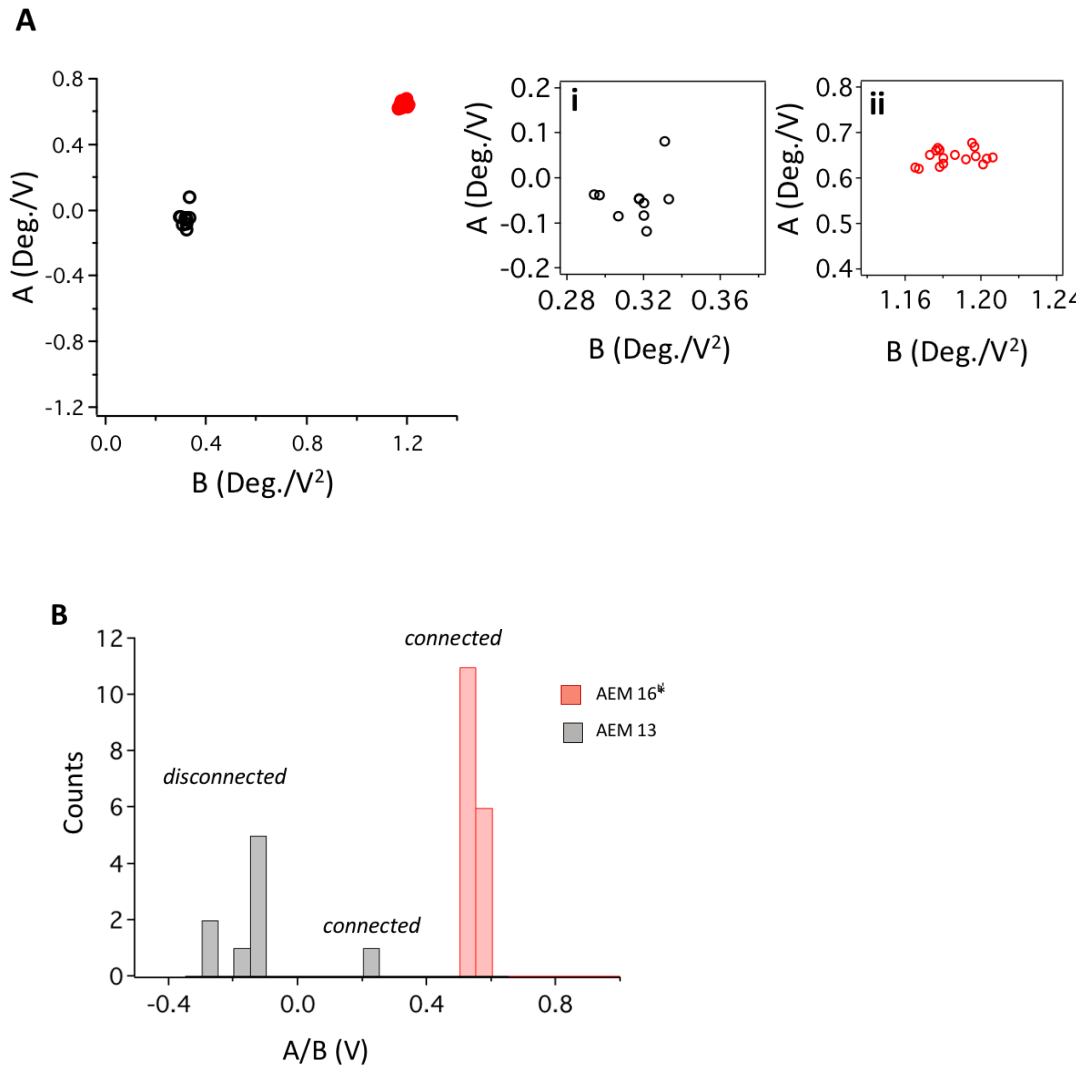


Figure 4: (A) Scatter plot of the linear fit term A vs. quadratic fit term B for several features of AEM 13 in black circles and AEM 16 in red circles. Inset shows a close-up of the scatter plot (A-i) AEM 13 and (A-ii) AEM 16. (B) Histogram of A/B data from (4A) for AEM 13 (gray) and AEM 16 (red).

We continued our investigation of the distribution and parabolic EFM behavior of several ionic domains on AEM 13 and AEM-16. It is important to note that not all ionic domains were able to be analyzed due to topographic artifacts. These topographical artifacts can contribute to the EFM phase and were thus avoided. A detailed discussion about how we discriminated these channels has been described previously.²⁵ In the EFM images that correspond to 3A-C, 10 regions of interest were analyzed, while 17 regions of interest were analyzed for 3D-F. Figure 4A shows scatter plots of fit parameter A vs. B for all channels analyzed for AEM 13 and AEM 16, respectively. The inset scatter plots show a close-up of the data highlighting the difference in variance of AEM 13 (A-i) and AEM 16 (A-ii). For AEM 13, points distribute near $A = 0^\circ/\text{V}$ and $B = 0.31^\circ/\text{V}^2$, while for AEM 16 the fit parameters can be seen near $A = 0.65^\circ/\text{V}$ and $B =$

$1.18^\circ/V^2$. The increase in both fit parameters A and B from AEM 13 to AEM 16 is due to increased IEC. A larger IEC would increase the total amount of stored charge of the membrane film and thus increase A, according to Eq. (4). An increase in the IEC would also make the membrane more polarizable, which would lead to an increase in B according to Eq. (3).

It is important to note that Eq. 3-5 also indicate a dependency on the film thickness. Control experiments in which the A and B values were measured of thick drop-cast and thin spun-cast films of un-quaternized membranes are shown in the Supporting Information. The un-quaternized membranes have an IEC of 0 mmol/g and thus contain no mobile charge. The control measurements indicate that decreasing the film thickness at constant charge leads to smaller values of A/B which is in agreement with Eq 5. Since the increase in A/B from AEM 13 (thick film) and AEM 16 (thin film) is due to the increase in IEC, the IEC plays a more significant role in the measurement of A/B than film thickness.

Figure 4B shows a histogram of A/B for AEM 13 and AEM 16 regions. AEM 13 shows a broad distribution with a cluster of points below $A/B = 0$, while AEM 16 shows a narrow distribution of $A/B > 0$. The variance in the distribution of A/B is attributed to the variation in channel connectivity. We have recently made a similar analysis to investigate the channel connectivity of Nafion.²⁵ Since the shape of the hydrophilic channels can be approximated as cylinders,¹² we could use the isolated cylinder model to interpret our EFM data. In the isolated cylinder model, A is proportional to the channel length.²⁶ Assuming that charge density is uniform, the variation in A/B is due to variations in channel length. Furthermore, the same model can be applied depending on whether cylinders lay parallel²¹ or perpendicular.^{22,26} Thus, we were able to conclude that only 1 out of 10 regions of AEM 13 led to a connected channel, while the rest were dead-end channels, and for AEM 16, all regions analyzed led to connected channels, as expected for perpendicular aligned channels.

CONCLUSIONS

Two AEMs with different IEC were investigated. AEM 13 with low IEC showed a mixture of parallel and perpendicular alignment of channels in the bulk though only parallel alignment on the surface. By contrast, for AEM 16 with high IEC, perpendicularly aligned channels were observed throughout the bulk and surface. From EFM phase images of both membranes, the EFM phase shift as a function of voltage bias was measured over the ionic domains. From the investigation on the parabolic EFM behavior as a function of voltage bias for the two membranes, variation was observed in the parabolic response of AEM 13 while very little variation was shown in AEM 16. These results suggest that there are a significant number of disconnected channels as a result of the parallel alignment observed in AEM 13, while for AEM 16, highly ordered structure of perpendicular channel alignment leads to a dominant population of connected channels.

REFERENCES:

- (1) Merle, G.; Wessling, M.; Nijmeijer, K. Anion Exchange Membranes for Alkaline Fuel Cells: A Review. *J. Memb. Sci.* **2011**, 377 (1–2), 1–35. <https://doi.org/10.1016/J.MEMSCI.2011.04.043>.
- (2) Varcoe, J. R.; Atanassov, P.; Dekel, D. R.; Herring, A. M.; Hickner, M. A.; Kohl, P. A.; Kucernak, A. R.; Mustain, W. E.; Nijmeijer, K.; Scott, K.; et al. Anion-Exchange Membranes in Electrochemical Energy Systems. *Energy Environ. Sci.* **2014**, 7 (10), 3135–3191. <https://doi.org/10.1039/C4EE01303D>.
- (3) Hickner, M. A.; Herring, A. M.; Coughlin, E. B. Anion Exchange Membranes: Current

- Status and Moving Forward. *J. Polym. Sci. Part B Polym. Phys.* **2013**, *51* (24), 1727–1735. <https://doi.org/10.1002/polb.23395>.
- (4) John R. Varcoe, *, †; Robert C. T. Slade, †; Graham L. Wright, † and; Chen ‡, Y. Steady-State Dc and Impedance Investigations of H₂/O₂ Alkaline Membrane Fuel Cells with Commercial Pt/C, Ag/C, and Au/C Cathodes. **2006**. <https://doi.org/10.1021/JP064898B>.
 - (5) Grew, K. N.; Chiu, W. K. S. A Dusty Fluid Model for Predicting Hydroxyl Anion Conductivity in Alkaline Anion Exchange Membranes. *J. Electrochem. Soc.* **2010**, *157* (3), B327. <https://doi.org/10.1149/1.3273200>.
 - (6) Zawodzinski, T. A.; Derouin, C.; Radzinski, S.; Sherman, R. J.; Smith, V. T.; Springer, T. E.; Gottesfeld, S. Water Uptake by and Transport Through Nafion® 117 Membranes. *J. Electrochem. Soc.* **1993**, *140* (4), 1041. <https://doi.org/10.1149/1.2056194>.
 - (7) Paddison, S. J.; Paul, R. The Nature of Proton Transport in Fully Hydrated Nafion®. *Phys. Chem. Chem. Phys.* **2002**, *4* (7), 1158–1163. <https://doi.org/10.1039/b109792j>.
 - (8) Choi, P.; Jalani, N. H.; Datta, R. Thermodynamics and Proton Transport in Nafion. *J. Electrochem. Soc.* **2005**, *152* (3), E123. <https://doi.org/10.1149/1.1859814>.
 - (9) Weber, A. Z.; Newman, J. Modeling Transport in Polymer-Electrolyte Fuel Cells. *Chem. Rev.* **2004**, *104* (10), 4679–4726. <https://doi.org/10.1021/cr020729l>.
 - (10) Hsu, W. Y.; Gierke, T. D. Ion Transport and Clustering in Nafion Perfluorinated Membranes. *J. Memb. Sci.* **1983**, *13* (3), 307–326. [https://doi.org/10.1016/0013-8182\(83\)90081-5](https://doi.org/10.1016/0013-8182(83)90081-5).
 - (11) Laurent Rubatat, †; Anne Laure Rollet, †, ‡; Gérard Gebel, † and; Olivier Diat*, †. Evidence of Elongated Polymeric Aggregates in Nafion. **2002**. <https://doi.org/10.1021/MA011578B>.
 - (12) Schmidt-Rohr, K.; Chen, Q. Parallel Cylindrical Water Nanochannels in Nafion Fuel-Cell Membranes. *Nat. Mater.* **2007**, *7* (1), 75–83. <https://doi.org/10.1038/nmat2074>.
 - (13) Noonan, K. J. T.; Hugar, K. M.; Kostalik, H. A.; Lobkovsky, E. B.; Abruña, H. D.; Coates, G. W. Phosphonium-Functionalized Polyethylene: A New Class of Base-Stable Alkaline Anion Exchange Membranes. *J. Am. Chem. Soc.* **2012**, *134* (44), 18161–18164. <https://doi.org/10.1021/ja307466s>.
 - (14) Zhang, W.; Liu, Y.; Jackson, A. C.; Savage, A. M.; Ertem, S. P.; Tsai, T.-H.; Seifert, S.; Beyer, F. L.; Liberatore, M. W.; Herring, A. M.; et al. Achieving Continuous Anion Transport Domains Using Block Copolymers Containing Phosphonium Cations. *Macromolecules* **2016**, *49* (13), 4714–4722. <https://doi.org/10.1021/acs.macromol.6b00653>.
 - (15) Sing, C. E.; Zwanikken, J. W.; Cruz, M. O. de la. Electrostatic Control of Block Copolymer Morphology. *Nat. Mater.* **2014**, *13* (7), 694–698. <https://doi.org/10.1038/nmat4001>.
 - (16) Park, M. J.; Kim, S.; Minor, A. M.; Hexemer, A.; Balsara, N. P. Control of Domain Orientation in Block Copolymer Electrolyte Membranes at the Interface with Humid Air. *Adv. Mater.* **2009**, *21* (2), 203–208. <https://doi.org/10.1002/adma.200801613>.
 - (17) O’Dea, J. R.; Buratto, S. K. Phase Imaging of Proton Exchange Membranes under Attractive and Repulsive Tip–Sample Interaction Forces. *J. Phys. Chem. B* **2011**, *115* (5), 1014–1020. <https://doi.org/10.1021/jp108821j>.
 - (18) Tamayo, J.; García, R. Relationship between Phase Shift and Energy Dissipation in Tapping-Mode Scanning Force Microscopy. *Appl. Phys. Lett.* **1998**, *73* (20), 2926. <https://doi.org/10.1063/1.122632>.

- (19) Oksana Cherniavskaya; Liwei Chen; Vivian Weng, †; Leonid Yuditsky, ‡ and; Brus*, L. E. Quantitative Noncontact Electrostatic Force Imaging of Nanocrystal Polarizability. **2003**. <https://doi.org/10.1021/JP0265438>.
- (20) Yalcin, S. E.; Labastide, J. A.; Sowle, D. L.; Barnes, M. D. Spectral Properties of Multiply Charged Semiconductor Quantum Dots. *Nano Lett.* **2011**, *11* (10), 4425–4430. <https://doi.org/10.1021/nl2026103>.
- (21) Malvankar, N. S.; Yalcin, S. E.; Tuominen, M. T.; Lovley, D. R. Visualization of Charge Propagation along Individual Pili Proteins Using Ambient Electrostatic Force Microscopy. *Nat. Nanotechnol.* **2014**, *9* (12), 1012–1017. <https://doi.org/10.1038/nnano.2014.236>.
- (22) Heim, T.; Lmimouni, K.; Vuillaume, D. Ambipolar Charge Injection and Transport in a Single Pentacene Monolayer Island NANO LETTERS. **2018**, *4* (11), 38. <https://doi.org/10.1021/nl0487673>.
- (23) Schaadt, D. M.; Yu, E. T.; Sankar, S.; Berkowitz, A. E. Charge Storage in Co Nanoclusters Embedded in by Scanning Force Microscopy. *Cit. Appl. Phys. Lett* **1999**, *74*, 472. <https://doi.org/10.1063/1.123039>.
- (24) Michael Jaquith; Erik M. Muller, † and; Marohn*, J. A. Time-Resolved Electric Force Microscopy of Charge Trapping in Polycrystalline Pentacene. **2007**. <https://doi.org/10.1021/JP073626L>.
- (25) Barnes, A. M.; Buratto, S. K. Imaging Channel Connectivity in Nafion Using Electrostatic Force Microscopy. *J. Phys. Chem. B* **2018**, *122* (3), 1289–1295. <https://doi.org/10.1021/acs.jpcc.7b08230>.
- (26) Mélin, T.; Diesinger, H.; Deresmes, D.; Stiévenard, D. Electric Force Microscopy of Individually Charged Nanoparticles on Conductors: An Analytical Model for Quantitative Charge Imaging. *Phys. Rev. B* **2004**, *69* (3), 035321. <https://doi.org/10.1103/PhysRevB.69.035321>.
- (27) Fang, S. J.; Haplepete, S.; Chen, W.; Helms, C. R.; Edwards, H. Analyzing Atomic Force Microscopy Images Using Spectral Methods. *J. Appl. Phys.* **1998**, *82* (12), 5891. <https://doi.org/10.1063/1.366489>.
- (28) Mclean, R. S.; Sauer, B. B. *Tapping-Mode AFM Studies Using Phase Detection for Resolution of Nanophases in Segmented Polyurethanes and Other Block Copolymers*; 1997.
- (29) Hasegawa, H.; Hashimoto, T. Morphology of Block Polymers near a Free Surface. *Macromolecules* **1985**, *18* (3), 589–590. <https://doi.org/10.1021/ma00145a051>.
- (30) Bates, F. S.; Fredrickson, G. H. Block Copolymer Thermodynamics: Theory and Experiment. *Annu. Rev. Phys. Chem.* **1990**, *41* (1), 525–557. <https://doi.org/10.1146/annurev.pc.41.100190.002521>.
- (31) Khanna, V.; Cochran, E. W.; Hexemer, A.; Stein, G. E.; Fredrickson, G. H.; Kramer, E. J.; Li, X.; Wang, J.; Hahn, S. F. Effect of Chain Architecture and Surface Energies on the Ordering Behavior of Lamellar and Cylinder Forming Block Copolymers. *Macromolecules* **2006**, *39* (26), 9346–9356. <https://doi.org/10.1021/ma0609228>.
- (32) Kim, S.; Briber, R. M.; Karim, A.; Jones, R. L.; Kim, H.-C. Environment-Controlled Spin Coating To Rapidly Orient Microdomains in Thin Block Copolymer Films. *Macromolecules* **2007**, *40* (12), 4102–4105. <https://doi.org/10.1021/ma0625298>.
- (33) Gu, X.; Gunkel, I.; Hexemer, A.; Russell, T. P. Controlling Domain Spacing and Grain Size in Cylindrical Block Copolymer Thin Films by Means of Thermal and Solvent Vapor Annealing. *Macromolecules* **2016**, *49* (9), 3373–3381.

- <https://doi.org/10.1021/acs.macromol.6b00429>.
- (34) Mélin, T.; Zdrojek, M.; Brunel, D. Electrostatic Force Microscopy and Kelvin Force Microscopy as a Probe of the Electrostatic and Electronic Properties of Carbon Nanotubes. In *Scanning Probe Microscopy in Nanoscience and Nanotechnology*; Springer, Berlin, Heidelberg, 2010; pp 89–128. https://doi.org/10.1007/978-3-642-03535-7_4.